JOURNAL OF GEOPHYSICAL RESEARCH, VOL. 89, NO. C4, PAGES 6453–6465, JULY 20, 1984

Spatial and Temporal Transformation of Shallow Water Wave Energy

SASITHORN ARANUVACHAPUN[1] AND EDWARD B. THORNTON

Department of Oceanography, Naval Postgraduate School

The surface wave spectra from the Atlantic Ocean Remote Sensing Land-Ocean Experiment (ARSLOE), during the passage of a 26-hour storm, were subjected to an empirical eigenfunction analysis. Results from the analysis are interpreted as the spatial and temporal variation of surface gravity waves propagating from deeper water into the shallow region where breaking finally occurs. The temporal variation is found to be approximately 7–17% of the total variance in the data and is considered as stochastic, with a fluctuation of about 2–3 cycles that appear correlated with the variation of the atmospheric forcing. The spatial variation (1–3%) is significantly less than the temporal variation but exhibits a deterministic part, indicating that the wave processes associated with the spatial variation can be considered deterministic. The principal eigenfunctions obtained from the analysis provide a good representation of the principal variations in the wave spectra as shown by the first eigenvalue of the covariance matrices. The radiative transfer equation is projected onto the eigenvector space, and the source function obtained from the suitable projection function is presented. By using the information extracted from the empirical eigenfunction analysis, various source functions for the wave field are inferred. The source functions evaluated in the present study are associated with the wave mechanisms of refraction and shoaling, atmospheric input, bottom friction, and wave-wave nonlinear interaction. The functions provide a good picture of the spectral wave energy balance, although further development of the current work can provide more detailed information about the energy transfer and may enhance the present picture of wave energy balance in the shallow water.

1. INTRODUCTION

Since our knowledge of the principal processes controlling the energy balance of the surface wave spectrum remains incomplete, numerical wave prediction models have to rely on a synthesis of empirically derived information from wave measurements. Without much consideration for the physical wave processes and energy transfer of the wave field, most empirical models tend to suffer a poor degree of accuracy. However, as more wave measurements have become available, models of the spectral wave energy balance have been successfully improved. The parametric wave prediction model of *Hasselmann et al.* [1976] (hereafter called PWPM) is an example of the improvement of wave prediction models based on the energy transfer equation. The model is essentially a function containing five free parameters, two scale parameters, and three shape parameters that fits closely to nearly all fetch-limited frequency spectra measured during the Joint North Sea Wave Project (JONSWAP) [*Hasselmann et al.*, 1973]. *Hasselmann et al.* [1976] also show that it is possible to describe the wave field in terms of only two such parameters. The parameters are related to the source functions of the wave field by projecting the radiative transfer equation, or the energy balance equation, onto the parameter space with appropriate projection functions. Therefore, for known wave mechanisms associated with the spectral energy transfer and the corresponding spectral parameters, the PWPM can be used to predict the wave conditions. Since the wave growth mechanism and resonant wave-wave interaction have been thoroughly investigated by *Hasselmann et al.* [1973], both processes have been implemented in the original PWPM. The model has also been applied to the hindcast of wave spectra under rapidly varying wind fields during the JONSWAP 1973 [*Günther et al.*, 1979*a*] and the hindcast study of extreme wave conditions in the North Sea [*Ewing et al.*, 1979]. Although the results are generally found to be encouraging, *Günther et al.* [1979*a*] suggest three important improvements to the model: (1) the implementation of shallow water effects, (2) the incorporation of a directional relaxation time for turning winds, and (3) a physically more realistic algorithm for the transformation between wind, sea, and swell. Initial attempts at both items 2 and 3 have been made by *Günther et al.* [1981, 1979*b*]. The papers provide careful analyses of the subject matters.

The nonlinear and linear bottom interaction effects in shallow water have been examined by *Shemdin et al.* [1978] to estimate the rate of energy dissipation. In their computation of the energy balance equation, each source function used is a known expression derived from an individual mechanism, while the actual source functions associated with the measured wave field have not been examined. Although the improvement of item 1 has so far been addressed, the source functions of the wave field in a shallow region have not yet been thoroughly investigated.

Furthermore, each individual source function used in the energy balance equation is, in general, derived from an isolated mechanism. For example the atmospheric input source function is usually derived from the Miles-Phillips-type generation [*Miles*, 1957; *Phillips*, 1958], whereas the nonlinear wave-wave interaction source function tends to assume the Hasselmann-type nonlinear interactions [*Hasselmann*, 1968]. Thus a wave prediction model that relies on these kind of source terms, generally performs well in the growing wind sea environment where wave generation is the most dominant mechanism. For a wave field with more than one competing mechanism, additional source functions can be added to the energy balance equation. Nevertheless, each mechanism remains independent of each other. The source functions do not account for any interaction between mechanisms, despite their competition in the wave field. Therefore, questions arise concerning the accuracy of theoretical source functions in representing the actual wave energy transfers. If a measured wave field has several competing wave mechanisms as well as the

[1]Presently at Institute of Oceanographic Sciences, U.K.

Paper number 4C0375.
0148-0227/84/004C-0375$05.00

mechanism interactions, will the actual source functions computed from the wave field be different from the source functions theoretically derived from each independent mechanism? Without assuming certain wave processes in the wave field, what do the actual source functions representing the energy transfers look like?

Our present study is motivated by an attempt to answer some of the above questions as well as a need to understand the principal processes controlling the spectral wave energy balance in the shallow water, as addressed by *Günther et al.* [1979*a*]. However, the study requires the wave measurements that describe the spectral evolution in both time and space. The Atlantic Ocean Remote Sensing Land-Ocean Experiment (ARSLOE) [*Vincent and Lichy*, 1982], conducted at Duck, North Carolina, from October 6 to November 30, 1980, provides a large data base of wave measurements suitable for determining the spectral wave energy balance in a shallow water wave regime. The spatial and temporal transformation of wave energy as the waves propagate into the nearshore zone is well represented in the data collected during the experiment. Wave data from ARSLOE during the passage of a 26-hour storm (October 24–25, 1980) are studied by using the empirical eigenfunction analysis. It is found that more than 80% of the frequency wave spectrum can be fitted by the first empirical eigenfunction, and therefore the principal eigenvector is used to represent each frequency spectrum measured. Using a projection method similar to *Hasselmann et al.* [1973, 1976] and *Günther et al.* [1979*a*, *b*], the energy balance equation is projected onto the eigenvector space. Since there is a lack of specific source term measurements, such as precise wind field measurements, the source terms are treated as unknowns. The unknown source terms are also projected with an appropriate projection function, which enables them to be solved. The objectives of this study are (*a*) to establish an algorithm for estimating the actual source terms from a measured wave field in the nearshore region; (*b*) to derive information concerning the energy transfer of the wave field; and (*c*) to use the information to infer the principal processes controlling the spectral wave energy balance in the shallow water.

The paper briefly describes the ARSLOE data acquisition and the measured wave field. The empirical eigenfunction analysis of the frequency wave spectra is presented where the results are interpreted in terms of spatial and temporal variation of spectral wave energy. Since the data were collected during the storm period, the temporal variation is found to be considerably larger than the spatial variation. The energy balance equation, its projection onto the eigenvector space, and the source functions are developed. Results from the computations of the source functions exhibit interesting variability of the source terms, which are used to infer the spectral energy transfer of the wave field, and the physical wave processes that might attribute to the energy transfer. An attempt has also been made to identify the principal physical processes modifying the wave field in this shallow water regime by using the qualitative spectral shapes of the source functions.

2. DESCRIPTION OF WAVE FIELD

The ARSLOE was conducted near the U.S. Army Coastal Engineering Research Center's ocean pier at Duck, North Carolina [*Vincent and Lichy*, 1982]. During the experiment a large low-pressure storm system occurred from October 23–25, 1980, with maximum sustained wind of greater than 15 m/s and significant wave heights up to 5 m. The wave data selected for our analysis were measured during the time of the storm. The measurements were acquired by using a transect of five wave-rider buoys between 12 and 0.7 km offshore and a line of seven Baylor wave gages attached to the 600-m pier in 9 to 1.3 m of water (see Table 1). The wave-rider buoys were pre- and post-calibrated. According to *Ribe* [1981], the total instrumentation error was estimated to be less than 4%. The error analysis includes the buoy sensitivity and the instrumentation drift caused by temperature variation. The Baylor gages and the pressure sensors are typically 99% accurate. Simultaneous wind measurements were obtained by using an anemometer located at the shoreline 19 m above MSL. The waves and wind were measured for 20 min every 2 hours throughout the experiment. The wave spectra were calculated for all the wave sensors given in Table 1. There are 13 time intervals during the period of 26 hours when wave spectra of all the sensors were computed. The wave measurements were digitally sampled at 0.25 s, resulting in a Nyquest frequency of 2.0 Hz. Spectra were obtained by dividing the 20-min records into 36 segments and applying a Fast Fourier Transform (FFT) algorithm to each segment. The raw spectra were averaged by frequency band to yield an averaged spectrum. The resulting spectra have 72 degrees of freedom with a resolution of 0.03125 Hz.

To illustrate the environments of the wave field during the storm, the rms wave heights for selected wave gages are plotted along with the mean sea level depicting variations caused by tide, wind speed, and direction (Figure 1). The winds were generally in the 10 to 15 m/s range, and they were initially from the northeast (winds directly onshore at Duck are from the ENE at 70° azimuth). As the extratropical low moved up the east coast, followed by a cold front passage, the winds turned clockwise until finally blowing offshore. The sea responded to the intensified winds with the waves growing to a maximum of 5 m on October 25, 1980 and then decaying as the winds shifted around to offshore direction.

As the waves propagate shoreward, there is a general decrease in wave height (and hence energy) as can be seen in Figure 1. The decrease in energy can be attributed to dissipation and/or wave divergence. The dissipation of wave energy can be attributed to the mechanisms of bottom friction, wave breaking percolation, coupled wave-bottom motions, sediment transport, and bottom scattering. For shoaling on a shallow shelf composed of fine grain sand, bottom friction would be expected to be the dominant dissipative mechanism prior to wave breaking [*Shemdin et al.*, 1978]. Once the waves start to break, turbulent dissipation caused by breaking becomes the dominant mechanism. The bathymetry about the

TABLE 1. Details of the Instruments and Their Locations

Instrument ID	Type	Distance From Baseline (on-offshore), m	Distance From Pier Centerline (alongshore), m	Depth relative to MSL, m
615	Baylor	189.0	0.0	1.3
635	Baylor	213.0	0.0	2.4
645	Baylor	238.0	0.0	3.8
655	Baylor	274.0	0.0	5.5
665	Baylor	323.0	0.0	5.7
621	pressure	620.0	110.0	6.0
675	Baylor	433.0	0.0	6.3
625	Baylor	579.0	0.0	9.1
620	wave rider	3,250	−44.0	17.1
630	wave rider	6,090	−490.0	18.9
710	wave rider	12,400	−510.0	21.3
730	wave rider	12,040	500	22.3
720	wave rider	12,270	−1,290.0	23.5

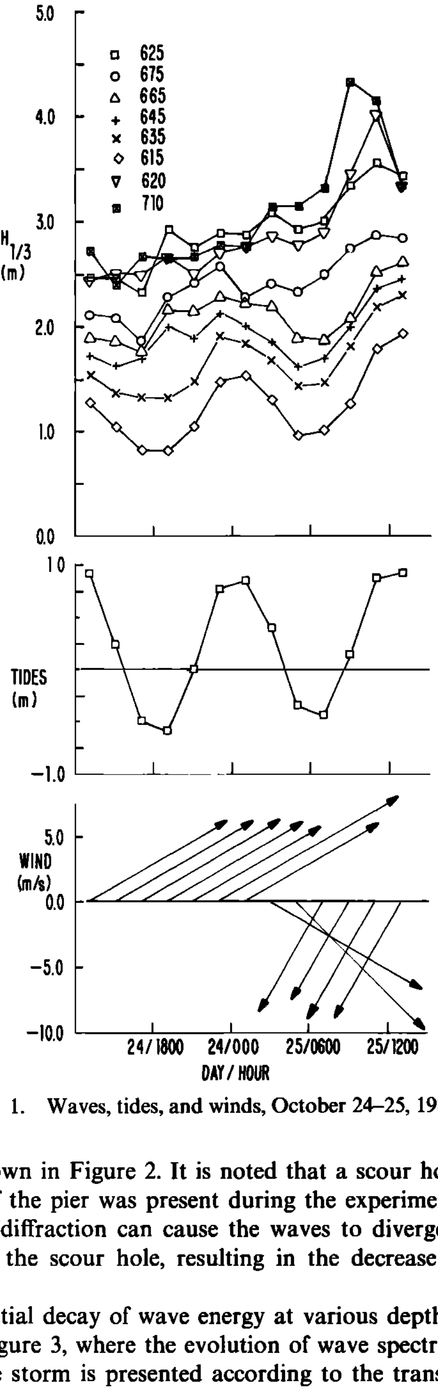

Fig. 1. Waves, tides, and winds, October 24–25, 1980.

pier is shown in Figure 2. It is noted that a scour hole about the end of the pier was present during the experiment. Wave refraction/diffraction can cause the waves to diverge as they pass over the scour hole, resulting in the decrease of wave height.

The spatial decay of wave energy at various depths can be seen in Figure 3, where the evolution of wave spectra in time during the storm is presented according to the transect from deep water to very shallow region. The spectra show a general decrease in energy across all spectral bands as the waves proceed shoreward. The temporal changes appear to reflect the variation in the wind field. Initially, the energy density has a maximum at 0.155 Hz. As the storm intensifies and the winds shift more onshore, the energy density grows with an increasing lower frequency. Swell at 0.123 Hz may be seen in Figure 3*a*. The higher-frequency sea waves (0.248 Hz) also reach a maximum on the 24th (or the 7th time interval) and then decrease as the winds shift around to the south.

The dependence of waves on the bottom topography is apparent in Figure 3(*b*, *c*), where refraction and shoaling are depicted respectively. The spectra presented in Figure 3*b* are from the area of the scour hole, and a divergence of wave energy is evident. Figure 3*d* shows dominant energy dissipation caused by wave breaking, where the time evolution of the spectra has much less energy than the deeper water (Figure 3*a* or 3*b*) and is more variable than the shallower water (Figure 3*e*). As the waves progress across the surf zone they become more and more depth limited, such that in the inner surf zone their height is approximately proportional to the depth [*Thornton and Guza*, 1982]. When waves begin to break, the breaking is primarily a function of wave height and water depth. Figure 3*e* represents an after-breaking situation when the waves appear to follow the tidal elevation. It is evident from the wave measurements in Figure 1 (also in Figure 3*e*) that the wave heights in the inner surf zone are almost independent of the offshore conditions and primarily dependent on the local depth.

3. Empirical Eigenfunction Analysis of Frequency Wave Spectra

An empirical eigenfunction analysis was selected to analyze the ARSLOE wave measurements, which are essentially the time series of the spatially varying wave field. The technique has been extensively used in analysis of data with more than one independent variable [e.g., *Wang and Mooers*, 1977; *Wallace and Dickinson*, 1972; *Aranuvachapun and Johnson*, 1979]. In particular the method is useful in discerning which part of the variability is related to temporal or spatial processes. The empirical eigenfunction analysis not only allows the variance distribution of the data to be represented by the empirical eigenvalues but also provides some information concerning the stochastic and deterministic properties of the data. Furthermore, the principal eigenfunction can represent the principal structure of the data, which is important since the representation is very useful for both data interpretations and modeling purposes. The analysis is applied to the wave spectral evolution. The wave spectra form arrays at the regular resolution interval of 3.125×10^{-2} Hz from 0.025 Hz to 0.650 Hz (or from 40.0-s to 1.5-s periods, respectively). Only the sea-swell band of wave transformation is to be examined. The spectral densities are stored in three-dimensional arrays whose x axes represent frequency, y axes represent the spatial distribution of the instruments, and z axes represent the time series. Figure 4 illustrates the frame of reference used for storing the digitized data as described. At a particular time the three-dimensional block of data is reduced to a two-dimensional data matrix A on the xy plane (see also Figure 4), where the columns represent discrete frequencies and the rows represent distances between two instruments along the transect from shallow water to deep region. There are 13 data matrices of A

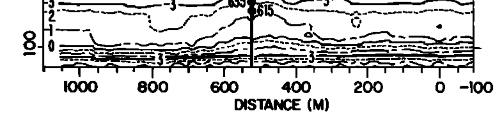

Fig. 2. Bathymetry about the pier at Coastal Engineering Research Center, Duck, North Carolina, October 1980.

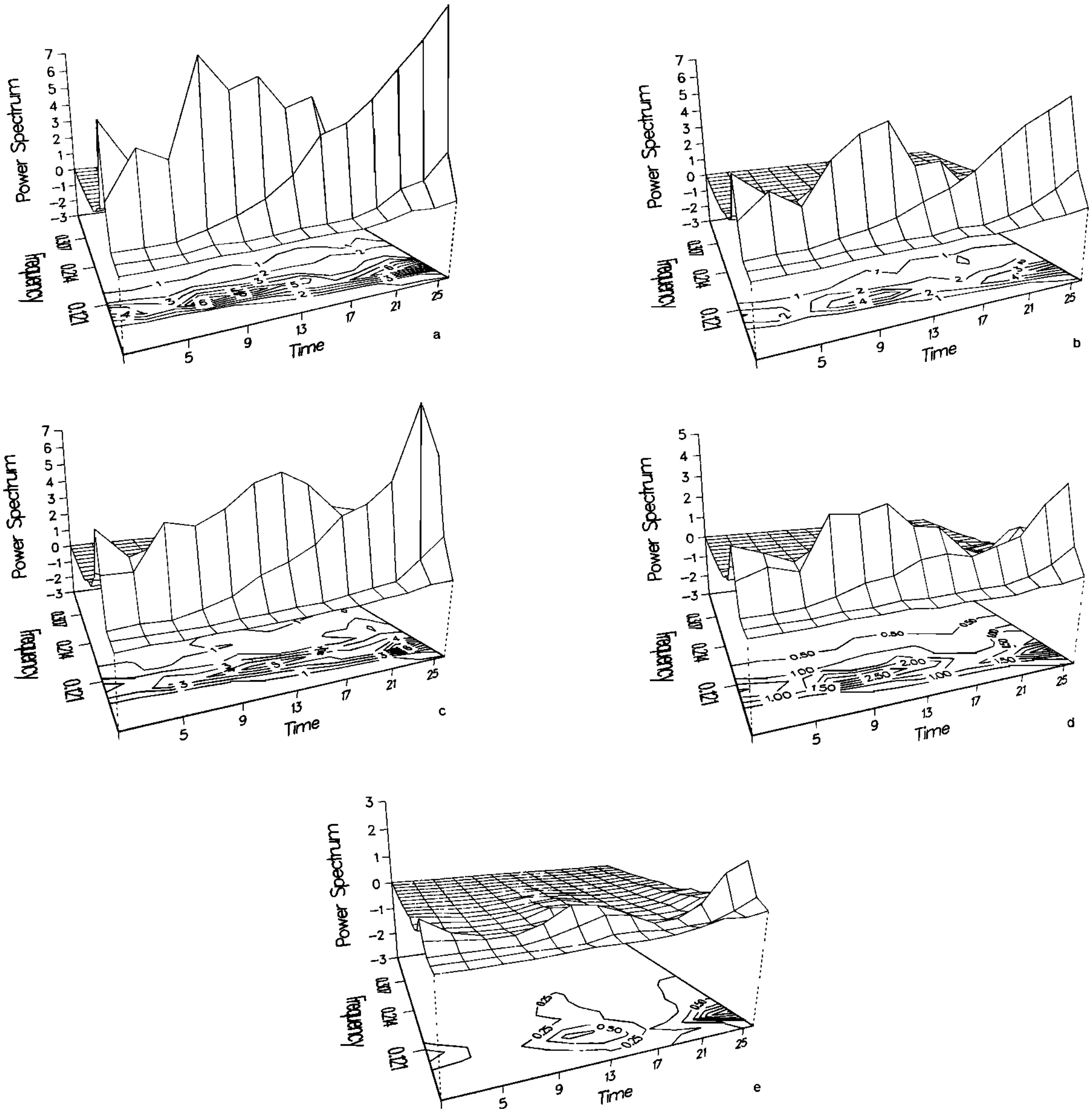

Fig. 3. Wave spectra as a function of time at (*a*) 18-m depth, (*b*) 10-m depth, (*c*) 7-m depth, (*d*) 6-m depth, (*e*) 2-m depth.

according to 13 realizations. Similarly, at a constant space the block of data is sliced horizontally along the xz plane to provide a two-dimensional data matrix B (see also Figure 4), where the columns still represent the same discrete frequencies, but the rows represent time scale. Because each data block has 13 discrete distances, there are also 13 data matrices of B.

Each data matrix of A is used to compute two covariance matrices P and Q, given by the following expressions:

$$P = \frac{A^T A}{ch}$$

where

$$P_{kl} = \frac{1}{ch} \sum_{i=1}^{h} a_{ik} a_{il} \qquad k, l = 1, 2, \ldots, c$$

and

$$Q = \frac{A A^T}{ch}$$

where

$$Q_{kl} = \frac{1}{ch} \sum_{j=1}^{c} a_{kj} a_{lj} \qquad k, l = 1, 2, \ldots, h$$

where A^T is the transpose of A, h is the number of discrete frequencies that is 20 in our present analysis, and c is the number of discrete distances that is 13. Similarly, two covariance matrices R and S are also computed from each data matrix B by using the same relations as above. Since P is essentially a sum over the frequency domain of the basic data, its eigenvalues and eigenvectors are associated with the spatial variation. The same consideration is applied to R, and therefore, its eigenvalues and eigenvectors are associated with temporal variation. Matrices Q and S are, again, sums over space and time domains, respectively, and so their eigenvalues and eigenvectors are associated with frequency spectra. Notice that, by reducing the three-dimensional data base to two dimensions, the interpretations of the resulting eigenvalues and eigenvectors are significantly simplified.

The P, Q, R, and S covariance matrices were fitted by em-

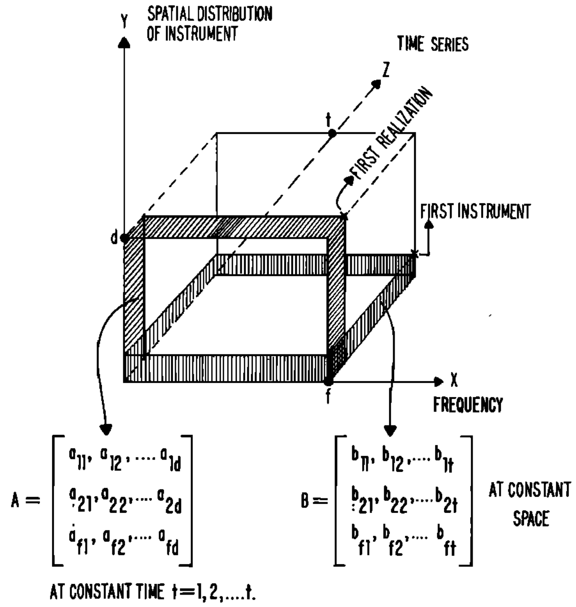

Fig. 4. Illustration of the frame of reference used for storing the spectral densities.

pirical eigenfunctions, and their eigenvalues and eigenvectors were computed. An example of the eigenvalues for covariance matrices P and Q calculated from data matrix A at a constant time (0715, October 25, 1980) is shown in Table 2, where the eigenvalues λ_n are well ordered so that $\lambda_1 > \lambda_2 > \lambda_3 \ldots$. Figure 5 illustrates a plot of eigenvalues against eigennumbers (or modes) that is known as an eigen index. Notice that the magnitude of λ_n decreases very rapidly as n increases (Table 2), and therefore, we will concentrate only on the first two eigenfunctions associated with the large leading eigenvalues λ_1 and λ_2. However, before attempting the interpretations of the results, certain properties of the empirical eigenfunctions should be stated as follows:

If the nth eigenvector u_n of P corresponding to the eigenvalue λ_n have components $u_{n1}, u_{n2}, \ldots, u_{nc}$ and the nth eigenvector v_n of Q have components $v_{n1}, v_{n2}, \ldots, v_{nh}$; then it can be shown that each wave spectrum may be represented as a linear combination of the v_{nj} in which the coefficients consist of the u_{ni} and λ_n. The appropriate formula for the energy density at ith instrument and jth frequency is

$$a_{ij} = \sum_{n=1}^{c} (ch\lambda_n)^{1/2} u_{ni} v_{nj}$$

The average over various instruments, or over space of a_{ij}, is

$$\frac{1}{c} \sum_{i=1}^{c} a_{ij} = \frac{1}{c} \sum_{i=1}^{c} \sum_{n=1}^{c} (ch\lambda_n)^{1/2} u_{ni} v_{nj}$$

$$= \sum_{n=1}^{c} (ch\lambda_n)^{1/2} \left\{ \frac{1}{c} \sum_{i=1}^{c} u_{ni} \right\} v_{nj}$$

Let $\bar{a}_j = 1/c \sum_{i=1}^{c} a_{ij}$ and $\bar{u}_n = 1/c \sum_{i=1}^{c} u_{ni}$. The above expression can be rewritten as

$$\bar{a}_j = \sum_{n=1}^{c} (ch\lambda_n)^{1/2} \bar{u}_n v_{nj} \qquad (1)$$

where $\bar{u}_n$ is the mean of the elements of u_n and $\bar{a}_j$ is the mean of the spectra at various eigenmodes. For $\lambda_1 \gg \lambda_2$ the leading term of (1) can give a good approximation to the frequency spectrum of spatial mean. Hence the spatial mean energy density function is approximated by the function

$$(ch\lambda_1)^{1/2} \bar{u}_1 v_{1j} \qquad j = 1, 2, \ldots, h \qquad (2)$$

Furthermore, the sum of the eigenvalue of the covariance matrix is equal to the mean square value of the data, i.e.,

$$\sum_{n=1}^{c} \lambda_n = \sum_{k=1}^{c} P_{kk} = \frac{1}{ch} \sum_{k=1}^{c} \sum_{i=1}^{h} a_{ik}^2$$

Thus, for centered data, the eigenvalue is the distribution of variance within the data. The largest eigenvalue λ_1 represents the greatest variability of the data; hence its corresponding eigenfunction, as given by (2) for λ_1, is termed the principal wave spectrum.

TABLE 2. The Eigenvalues of Covariance Matrices P and O Calculated From the Data Matrix A at the Constant Time of 0715, October 25, 1980

Mode n	Eigenvalues λ_n	Contribution Rate of λ_n, %	Accumulation Rate of λ_n, %
1	0.178E + 01	96.60	96.60
2	0.436E − 01	2.37	98.97
3	0.945E − 02	0.51	99.48
4	0.532E − 02	0.29	99.77
5	0.230E − 02	0.13	99.89
6	0.114E − 02	0.06	99.95
7	0.591E − 03	0.03	99.99
8	0.179E − 03	0.01	100.00
9	0.354E − 04	0.00	100.00
10	0.196E − 04	0.00	100.00
11	0.772E − 05	0.00	100.00
12	0.400E − 05	0.00	100.00
13	0.849E − 06	0.00	100.00

4. RESULTS AND INTERPRETATIONS

The computations of eigenfunctions of the form (2) for λ_1 and λ_2 were carried out, and the results are presented in Figure 6a, where the functions are plotted against the wave

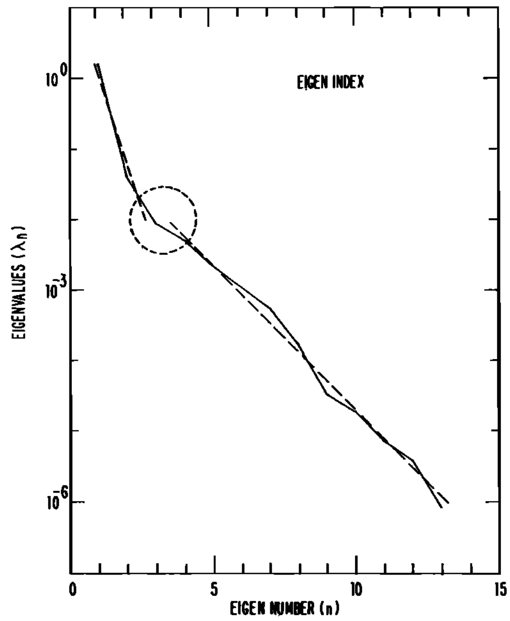

Fig. 5. Eigen index of the spatial evolution of the wave field at a constant time of 0715, October 25, 1980.

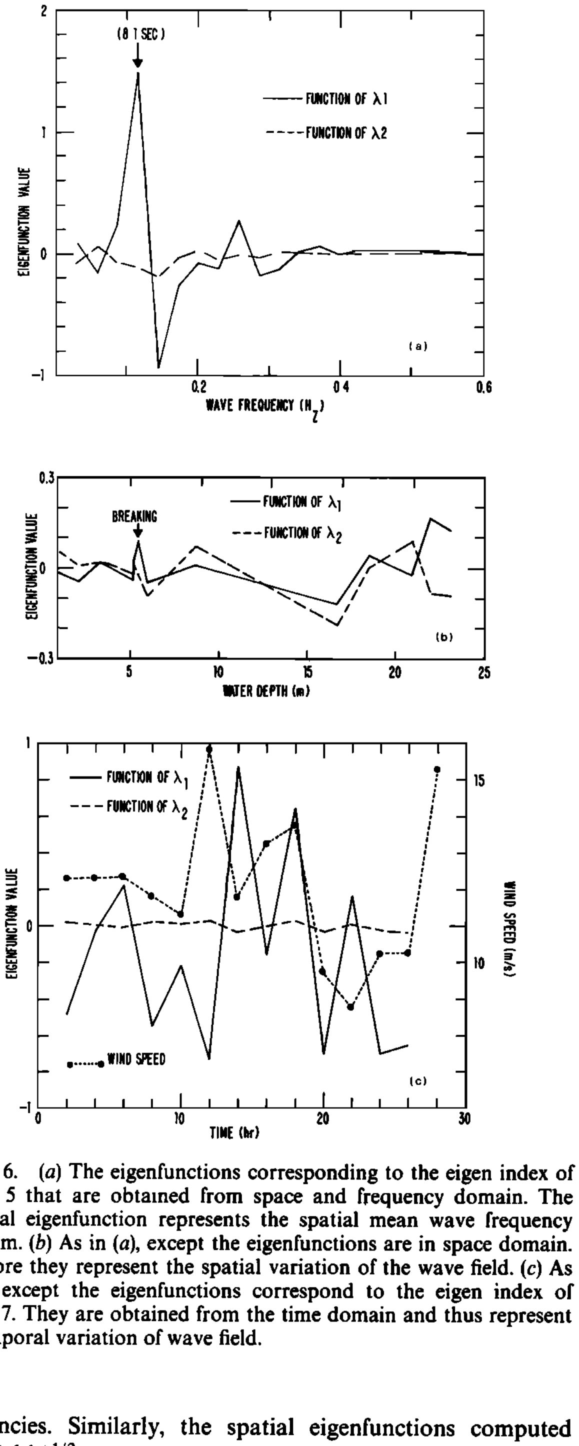

Fig. 6. (*a*) The eigenfunctions corresponding to the eigen index of Figure 5 that are obtained from space and frequency domain. The principal eigenfunction represents the spatial mean wave frequency spectrum. (*b*) As in (*a*), except the eigenfunctions are in space domain. Therefore they represent the spatial variation of the wave field. (*c*) As in (*a*), except the eigenfunctions correspond to the eigen index of Figure 7. They are obtained from the time domain and thus represent the temporal variation of wave field.

frequencies. Similarly, the spatial eigenfunctions computed from $(ch\lambda_n)^{1/2}\bar{v}_n u_{ni}$, $i = 1, 2, \ldots, c$, for the same λ_1 and λ_2 ($n = 1$ and 2) are presented in Figure 6*b*. The spatial eigenfunctions are plotted against the water depths. Notice that, from one data matrix A, two covariance matrices P and Q can be estimated, and they provide empirical eigenfunctions in space and frequency domains, respectively, that indicate the principal structures of the data and their orthogonal variations (see also Figure 6(*a*, *b*)). The same calculations were repeated for a data matrix B chosen at the constant depth of approximately 23 m, where two covariance matrices R and S provide the empirical eigenfunctions in time and frequency domains, respectively. The eigenvalues from R and S are tabulated in Table 3, while the eigen index is shown in Figure 7. The temporal eigenfunctions for λ_1 and λ_2, similar to the eigenfunctions shown in Figure 6*b*, are illustrated in Figure 6*c*, where the functions are plotted against the time series of the data in 26 hours. Although the analysis provides 26 sets of eigenvalues (eigen indices) and 52 sets of eigenfunctions, the interpretations will be focused on the results from the above examples, which are selected to represent typical cases of the data. The interpretations are summarized as follows:

4a. *Properties of the Wave Field*

Preisendorfer et al. [1981] state that the eigenvalues of a system composed of both deterministic and stochastic processes can be expressed as

$$\lambda_k = \frac{1}{2}\beta_k^2 + \sigma_k^2 \qquad k = 1, 2, \ldots, n$$

where the deterministic part of the system has m degrees of freedom with amplitudes of oscillations β_i, $i = 1, 2, \ldots, m$, while the stochastic part has a standard derivation of σ_j, $j = 1, 2, \ldots, n$. For $m < n$ the eigenvalues for $k = m + 1, \ldots, n$ are essentially σ_k^2, since at $k = m$ the extra contribution on σ_k^2 from $\frac{1}{2}\beta_k^2$ stops and is missing for $k > m$. These n-m eigenvalues are the purely stochastic tails of the sequences that usually provide different decay rates than the earlier eigenvalues where the extra contribution from $\frac{1}{2}\beta_k^2$ is found. Thus there is a region where the changing of decay rate occurs, which is significant and generally detectable in a plot of the eigen index. For example, Figure 5 shows the dotted region where the changing of slope of the eigenvalue curve occurs, which implies that the processes associated with the wave propagation into shallow water are deterministic. Thus, wave mechanisms such as wave refraction and shoaling may produce deterministic properties of the wave field. On the other hand, Figure 7, which is similar to Figure 5, except the eigen index is for the data of time and frequency domain, does not show a slope-changing region. The curve seems to have a constant slope as shown by the dashed line, indicating that the temporal wind forcing of the waves is purely stochastic.

In general, results from the analysis suggest that almost 99% of the data is contained within the first seven modes of the empirical eigenfunction analysis as shown, for example, by the accumulative rate of the eigenvalues tabulated in both Tables 2 and 3; this indicates that the wave field exhibits a minimum of 7 degrees of freedom. Since the principal eigenfunction in the frequency domain generally contains more

TABLE 3. The Eigenvalues of Covariance Matrices R and S Calculated From the Data Matrix B at the Constant Depth of Approximately 23 m

Mode n	Eigenvalues λ_n	Contribution Rate of λ_n, %	Accumulation Rate of λ_n %
1	0.387E + 01	84.18	84.18
2	0.631E + 00	13.72	97.90
3	0.769E − 01	1.67	99.57
4	0.125E − 01	0.27	99.84
5	0.576E − 02	0.13	99.97
6	0.102E − 02	0.02	99.99
7	0.249E − 03	0.01	100.00
8	0.726E − 04	0.00	100.00
9	0.459E − 04	0.00	100.00
10	0.288E − 04	0.00	100.00
11	0.135E − 04	0.00	100.00
12	0.320E − 05	0.00	100.00
13	0.919E − 06	0.00	100.00

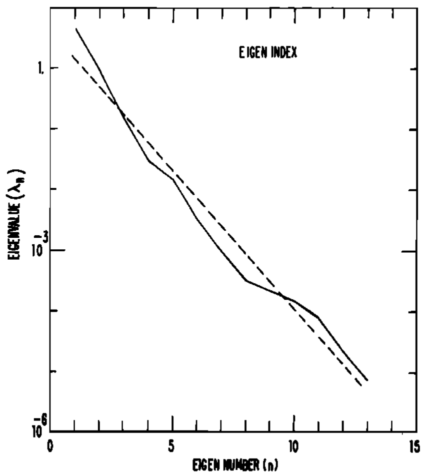

Fig. 7. Eigen index of the temporal evolution of the wave field at a constant depth of approximately 23 m. The index is obtained from the time and frequency domain.

than 80% of the variance, it gives an excellent approximation of the principal wave energy density spectrum. It is found from the eigenvalues of space and frequency domains that the significant spatial variation corresponding to λ_2 to λ_7 is approximately 1–3% of the variance, and it may be deterministic as suggested by the eigen index (see Figure 5). Likewise, from the eigenvalues of time and frequency domains it is found that the significant temporal variation is approximately 7–17% of the variance, and it could be stochastic with the fluctuation of about 2–3 cycles. The fluctuation tends to vary with wind speed, which will be further discussed in the next section.

4*b*. *Temporal and Spatial Variation of Wave Spectra*

Most of the principal wave spectra obtained from the frequency domain analysis generally exhibit a dominant peak at 0.12 Hz (8.1-s period) (see Figure 6*a* for example), except during the onshore high wind condition (wind speed greater than 15 m/s) when a dominant peak at 0.16 Hz (6.4-s period) is found. Waves at higher frequency can be generated by the wave growth mechanism, produced by strong surface wind, and the wave-wave resonant interaction. Both of these wave processes are well described and explained in *Hasselmann et al.* [1973]. Because the wave field was very energetic, another, smaller significant peak at 0.20–0.25 Hz (4–5 s period) in the high-frequency end is also found throughout the results from the analysis. Since the extreme high wind condition lasted for several hours, the significant wave energy at 0.16 Hz still remained in the proceeding records, and therefore, the peak at 0.16 Hz is found together with the dominant swell peak at 0.12 Hz in the corresponding principal eigenfunctions. The eigenfunctions associated with λ_2, in general, show a smaller amplitude of oscillation that decreases to almost zero with the increase in frequency, indicating that most of the variance in the spectra is well captured within the lower end of the frequencies.

Although the eigenvalues resulting from the analysis suggest that the magnitude of the spatial variation is approximately 1–3% of the total variance in the data, which is considerably smaller than the magnitude of the temporal variation, there are interesting features given by the principal eigenfunction in space domain. The typical features may be seen in Figure 6*b*, where large variations of wave spectra caused by water depth are found at depths 4–6 m and 17–22 m. The features are consistently found throughout the results and suggest that, at depth 4–6 m, the breaking of storm waves occurs and consequently causes a variation in very shallow water, while at depth 17–22 m, the refraction and shoaling of swell, which are wave processes associated with the energy dissipation caused by bottom topography, may occur, and therefore a large spatial variation could be found. Notice however, the eigenfunction of λ_2 tends to vary in a similar way as the principal eigenfunction (of λ_1), except at depths greater than 22 m, suggesting that there is no distinguished feature shown by the eigenfunction of λ_2 in the shallow water which can be used to infer any other physical wave process.

Because the measurements were made during a storm passage, the temporal variation is significantly higher, with its magnitude as large as 17% of the total variance in the data. The principal eigenfunction in the time domain generally illustrates 2–3 cycles of fluctuation over the 26 hours duration. The fluctuation is enhanced in deeper water where the depth is greater than 10 m, while in very shallow water the tidal oscillation tends to interfere and dominate the overall temporal variation. The temporal variation at depth 23 m exhibits a correlation with the fluctuation of wind speed. Figure 6*c* shows the temporal variation represented by the principal eigenfunction (of λ_1) in a solid line superimposed on the wind speed variation shown by the dotted line. Once again, the eigenfunction of λ_2 is small and insignificant compared to the principal eigenfunction (of λ_1).

5. Eigenvector Radiative Transfer Equation

In general, when the empirical eigenfunction analysis is applied to a data matrix, it is hoped that the eigenfunction corresponding to a particular eigenvalue will represent a certain variation used to infer a physical process in the data. The eigenvalue will also indicate the amount of the variance and the variance distribution. Then, for various eigenvalues and eigenfunctions, different mechanisms could be identified so that knowledge of these processes can be derived. However, our analysis indicates that the oscillation shown in each eigenfunction of the leading eigenvalues of the same domain is associated with several competing wave mechanisms, which are not separable by means of variance partition alone. This is clearly demonstrated by the eigenfunctions of λ_1 and λ_2 in the space domain, as shown in Figure 6*b*. Nevertheless, the principal eigenfunctions of frequency, space, and time domains are very useful in providing the principal structures of the wave field given by the data. The rates of change of the wave spectra with respect to time and space are the quantities needed in the calculations based on the energy balance equation. In particular, the principal wave spectrum, which contains more than 80% of the data variability, is a valuable representation of the measured wave spectra. Thus we use the principal wave spectrum in this study to represent the wave field so that the energy balance equation can be projected onto the eigenvector space. Other use of the principal wave spectrum may be found in *Vincent and Resio* [1977], where the empirical eigenfunction analysis is applied to the wave spectra only in the frequency domain. They show that a reconstruction of a spectrum to a good degree of accuracy only requires the first five modes of the empirical eigenfunctions.

The evolution in time (t) and space (x) of the one-dimensional energy density spectrum E (f; x, t) of surface gravity waves is governed by the radiative transfer equation (i.e., energy balance) of the form

$$\frac{DE}{Dt} = \frac{\partial E}{\partial t} + v_f \frac{\partial E}{\partial x} = \xi \tag{3}$$

where v_f is the group velocity of E at frequency f, and ξ is the source function that can be a summation of various source terms ($\xi = \xi_1 + \xi_2 + \ldots$). In our eigenfunction analysis the results indicate that for each measured spectrum there exists a class of eigenfunctions $E^*(u_1, u_2, \ldots, u_n; x, t)$ containing n independent components u_n that can represent the actual measured spectrum. There is also the algorithm for computing the component u_n for any given spectrum $E(f; x, t)$, and so we may write

$$u_j = \phi_j(E) \tag{4}$$

where the functional ϕ_j is differentiable, i.e., a small variation in E (denoted δ E) yields a small variation of the component u_j. Thus the functional derivative ϕ_j' is of the form

$$\delta u_j = \phi_j'(\delta E) \tag{5}$$

The expressions (4) and (5) together are our linear projection operator, which provides the relation [see *Hasselmann et al.* [1973, 1976] for examples)

$$\phi_i'\left(\frac{\partial E^*}{\partial u_j}\right) = \delta_{ij} \tag{6}$$

Since E can be approximated by E^* for all x and t, we may substitute E^* in the radiative transfer equation and write the equation in terms of eigenfunction components

$$\frac{\partial E^*}{\partial u_j}\left(\frac{\partial u_j}{\partial t} + v_f \frac{\partial u_j}{\partial x}\right) = \xi$$

The projection of the radiative transfer equation onto the eigenvector space is the same projection method used by *Hasselmann et al.* [1973, 1976]. The linear projection operator is now applied to the above expression and by invoking (6), the eigenvector radiative transfer equation takes the form

$$\frac{\partial u_i}{\partial t} + H_{ij} \frac{\partial u_j}{\partial x} = \xi_i \tag{7}$$

where

$$H_{ij} = \phi_i'\left(v_f \frac{\partial E^*}{\partial u_j}\right)$$

and

$$\xi_i = \phi_i'(\xi)$$

For the shallow water waves the group velocity is a smoothly varying function over depth, i.e., $v_f = (gd)^{1/2}$. (For deep water where $v_f = g/4\pi f$, this smoothly varying function may be replaced to its first order by the constant value of group velocity at the peak frequency [*Hasselmann et al.*, 1973].) The velocity v_f is essentially a constant over a finite narrow range of frequency, and therefore, we may drop the subscript f and rewrite the expression for H_{ij}, after invoking (6), as

$$H_{ij} = v\delta_{ij}$$

Substituting H_{ij} into (7), the eigenvector radiative transfer equation becomes

$$\frac{\partial u_i}{\partial t} + v \frac{\partial u_i}{\partial x} = \xi_i \tag{8}$$

The first and the second terms on the left side are essentially the rates of change of the principal eigenfunction in time and space domains, respectively. Both terms are known from the empirical eigenfunction analysis of the frequency wave spectra, and therefore, the term ξ_i on the right side of the expression is also known. Notice a significance of the analysis; it provides not only a good approximation of the principal structures of the wave data but also the quantitative spectral evolution. The latter is very essential in both wave predictions based on the energy balance equation and source function calculations, which will be discussed in the following section.

6. SOURCE FUNCTIONS

To solve for the source function ξ, the linear projection functional ϕ_i' is made more tractable by defining

$$\phi_i'(E) = \int_{f_1}^{f_2} \delta u_i E(f)\, df \qquad f_1 \le f \le f_2$$

which has a property

$$\int_{f_1}^{f_2} E(f)\, df = 1$$

The property implies that there is only a finite unit area of the spectrum that can be projected by the linear functional ϕ_i'. Similarly, we write

$$\phi_i'(\xi) = \int_{f_1}^{f_2} \delta u_i \xi(f)\, df$$

This projection function has the form of a Fredholm integral equation, which can be rewritten in the matrix form as [*Chambers*, 1976]

$$\Phi = \hbar U \xi \tag{9}$$

where Φ and ξ are column matrices with n elements of $\phi_i'(\xi)$ (or ξ_i) and $\xi(f)$, respectively. The square matrix U has dimension $n \times n$ with elements δu_i, whereas the constant length scale $\hbar$ is defined as

$$\hbar = \frac{f_2 - f_1}{n} > 0$$

The matrix equation (9) has a unique solution

$$\xi = (\hbar U)^{-1}\Phi \tag{10}$$

provided that U is a nonsingular matrix. Once again, the n elements of Φ are the same n elements of ξ_i that can be computed by using (8).

Computations of the source function ξ were carried out by using (10) and the Φ or ξ_i obtained from (8). The term $\partial u_i/\partial t$ was evaluated at two different constant depths of approximately 7 m and 23 m because the first depth represents the beginning of the surf zone, while the second depth is where the enhanced temporal variation is found. However, results of the computations show no significant difference between the two depths, and therefore $\partial u_i/\partial t$ at depth 7 m is selected for all the calculations. The term $\partial u_i/\partial x$ was evaluated at each constant time. The $n \times n$ square matrix U is the principal eigenvector component, which has been arranged in two distinct manners:

1. The principal eigenvector components in frequency and space domains, which represent the principal wave spectra, are arranged such that the columns denote the discrete frequencies while the rows denote the discrete realizations. Since the principal components in frequency and space domains ex-

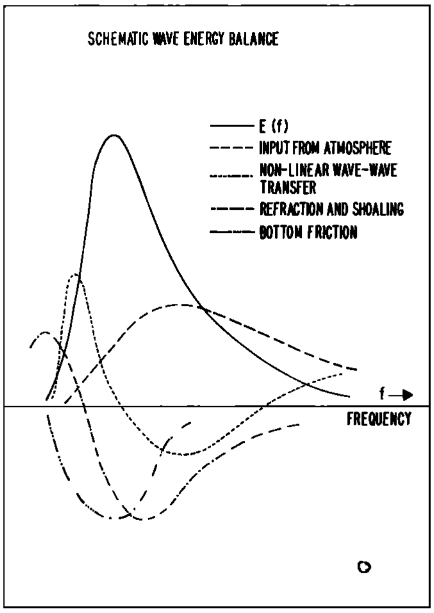

Fig. 8. Schematic wave energy balance for the energetic wave field in shallow water.

hibit the spatial variation of wave data, the matrix U constructed in this manner will also contain the inherent spatial variation. Thus the source function ξ computed from this type of matrix U is associated with the physical wave processes, such as shoaling and refraction, that are known to cause the spatial variation in wave field.

2. The principal eigenvector components in frequency and time domains are arranged similarly to 1, except the rows denote the discrete spacing of the instruments. Likewise, the principal components in frequency and time domains exhibit the temporal variation, and therefore, the matrix U constructed in this manner will have the inherent temporal variation that makes the source function ξ computed from this type of matrix U belong to the wave processes that generate the temporal variation. Examples of such processes are the transfer of momentum from wind to waves (the atmospheric input) and the wave-wave nonlinear interaction.

The computations were also repeated for different eigenvector components. The principal eigenvector was replaced by the summation of the eigenvectors corresponding to λ_2 to λ_7, and the matrix U was constructed following 1 and 2. To make the results of our calculations more tractable, we denote $\xi^{(a)}$ as the source function computed from the matrix U as constructed in 1 and similarly, $\xi^{(b)}$ for the matrix U as constructed in (2). We also denote $\xi^{(c)}$ as the source function computed from the sum of the eigenvectors corresponding to λ_2 to λ_7, where the matrix U is constructed following 1, and finally, $\xi^{(d)}$ for the similar matrix U but constructed following 2. Thus for each set of calculations there are four source functions representing different energy transfer processes provided by the variance partition in the data. The source functions offering information on the energy balance of the wave field are discussed as follows:

6a. *Theoretical and Computed Source Function*

A schematic wave energy balance is shown in Figure 8, where various source functions resulting from different physical wave processes are plotted against the frequency. The functions are synthesized from the information obtained in *Hasselmann et al.* [1973] and *Shemdin et al.* [1978]. Each source function is a theoretical estimate for a known independent process. There is no allowance for interactions between the processes. Such theoretical source functions are unlike the computed source functions presented here, since the latter functions make no assumption on the known independent wave process. Thus the computed source functions do account for the mechanism interactions as well as the existing mechanisms in the wave field. Figures 9–12 show the four computed source functions plotted against wave frequency for depths 2.0 m, 6.7 m, 18.5 m, and 24.4 m, respectively. Although the theoretical source functions shown in Figure 8 may not be directly comparable to the computed source functions shown in Figures 9–12, as a result of the different wave conditions and circumstances, the comparisons provide the most valuable discussion. It may be seen in general that $\xi^{(a)}$ agrees qualitatively with the schematic source function caused by refraction and shoaling as shown in Figure 8, while $\xi^{(b)}$ tends to agree with the source function of the atmospheric input. Similarly, the computed source function $\xi^{(c)}$ resembles qualitatively the shape of the theoretical source function of bottom friction, while $\xi^{(d)}$ generally agrees with the source function of nonlinear wave-wave transfer. Because of these similarities found in the comparisons, it is suggested that the source functions $\xi^{(a)}$, $\xi^{(b)}$, $\xi^{(c)}$, and $\xi^{(d)}$ obtained in this study might be associated with the following wave mechanisms respectively: refraction and shoaling, atmospheric input, bottom friction, and nonlinear transfer.

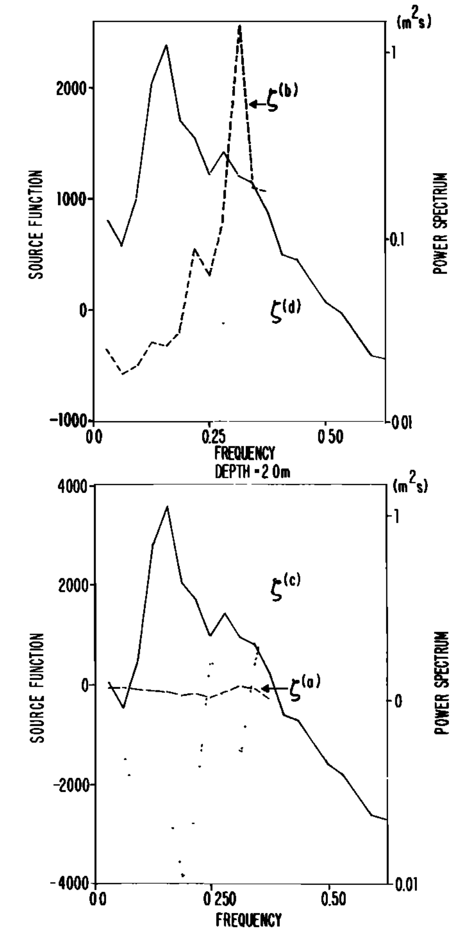

Fig. 9. Four different source functions $\xi^{(a)}$, $\xi^{(b)}$, $\xi^{(c)}$, and $\xi^{(d)}$ plotted against the frequency for depth of 2.0 m.

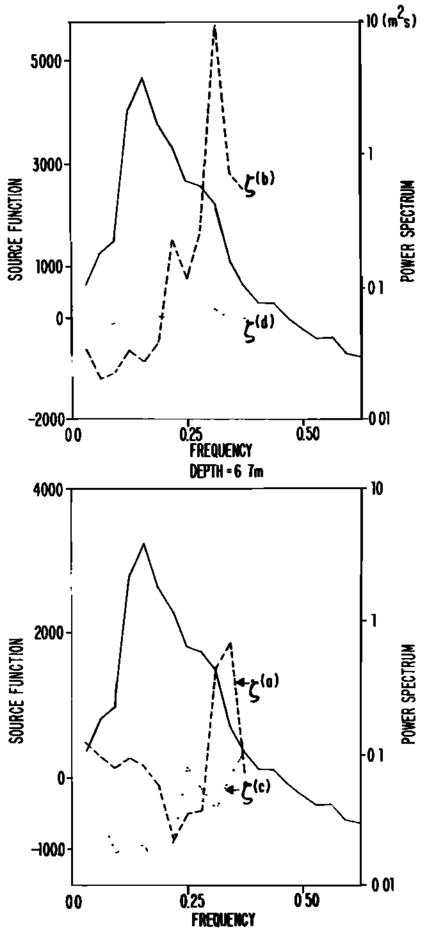

Fig. 10. As in Figure (9), except for depth of 6.7 m.

It must be noted that differences are also found in the comparisons. For example, in the high-frequency range ($f > 0.25$ Hz or the period less than 4 s) the computed source functions $\xi^{(a)}$ and $\xi^{(b)}$ do not agree well with their corresponding theoretical functions. The discrepancies could be attributed to the differences in the wave field environments and situations. The theoretical $\xi^{(b)}$ usually assumes the Miles-Phillips-type generation that neglects the effects caused by the rapid change of wind direction, whereas the computed source function $\xi^{(b)}$ includes the response of wave field caused by the rapid change of wind direction that occurred during the measurements. Also, the function $\xi^{(a)}$, which represents the energy balance caused by wave refraction and shoaling, depends on the topography of the nearshore region. Therefore, a discrepancy of the function as a result of different locations is to be expected. Furthermore, the computed source functions represent both the wave processes and their interactions. The latter is lacking in the theoretical source functions, and thus significant discrepancies between the computed and the theoretical functions are, once again, to be expected.

6b. *Variability of Computed Source Functions*

It is found that all the source functions for four different water depths (see also Figures 9–12), in general, exhibit consistent patterns of energy transfer within a wave spectrum, except the nonlinear transfer. The source function $\xi^{(d)}$ (representing nonlinear transfer) in very shallow water (depth less than 6 m) has a slightly higher value at the low-frequency end than at the high-frequency range, as can be seen in Figure 9, and the situation seems to reverse in deep water (see Figure 12), where the function has a higher value at the high-frequency end. The first situation suggests that in very shallow water the dominant nonlinear energy transfer is due to energy dissipation mechanisms such as breaking and interaction with bottom friction, which is enhanced at the lower frequencies. The situation is in agreement with the source function ($\xi^{(c)}$) in the same figure (Figure 9), indicating a large magnitude of bottom friction effects on the energy transfer. The latter situation (see Figure 12), however, indicates that in deep water the dominant nonlinear transfer of energy is the wave-wave interaction in the wave growth mechanism occurring at the high frequency. This ties in well with the atmospheric input source function ($\xi^{(b)}$) that shows a significant peak at approximately 3.2 s, indicating an active wave generation process. The response of the wave field to such an atmospheric input is evidently shown by the existence of the 4-s waves, which are found in most of the principal wave spectra, as discussed in the section 4*b*.

Although the energy transfer resulting from refraction and shoaling ($\xi^{(a)}$) and bottom friction ($\xi^{(c)}$) is found to be consistent throughout the depths (see Figures 9–12), the magnitude of the source function $\xi^{(a)}$ is largest at depth 18.5 m, as illustrated in Figure 11. It implies that at depth 18.5 m the low-frequency swell shoaled significantly, which consequently makes the energy dissipation caused by the bottom topography significant, as shown by the trough of the curve. The peak of the curve also implies an energy gain in the spectrum. Fur-

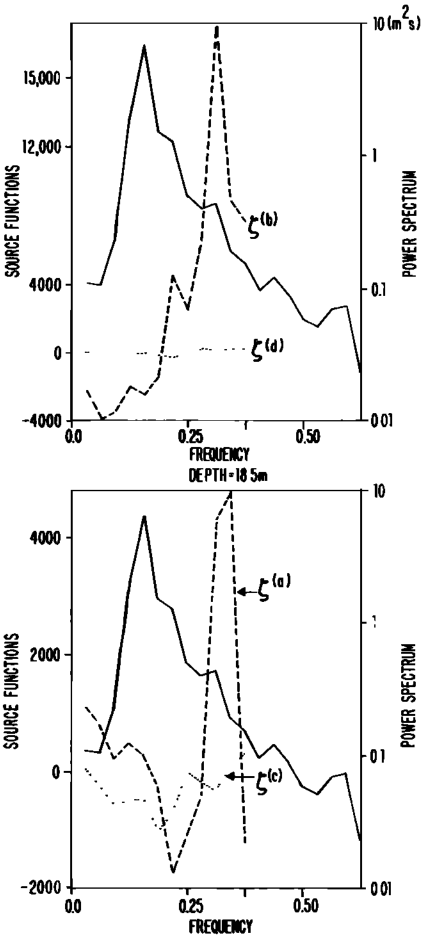

Fig. 11. As in Figure (9), except for depth of 18.5 m.

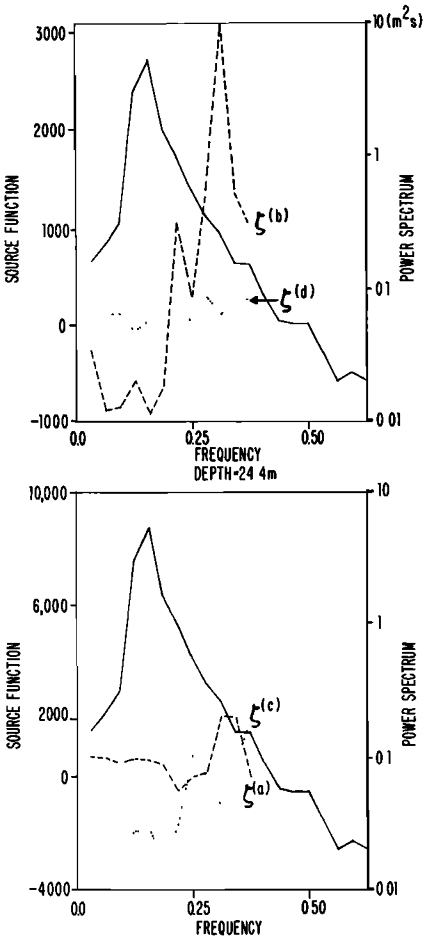

Fig. 12. As in Figure (9), except for depth of 24.4 m.

thermore, in the surf zone where breaking of waves is known to be pronounced, the bottom friction ($\xi^{(c)}$) is also found to be greatest, as can be seen in Figure 9. Notice that the energy transfer caused by wave breaking is not incorporated as an individual mechanism in the present study because our understanding of the breaking mechanism and its energy transfer has not yet been fully established. However, the energy transfer as shown by the source functions $\xi^{(a)}$ and $\xi^{(c)}$ at depths 2.0 m and 6.7 m, where breaking of wind waves could have occurred, should also represent partial energy transfer caused by breaking. Thus, although the functions are associated with refraction and shoaling and bottom friction beyond the surf zone and inside the surf zone, they also include the wave breaking energy transfer.

Since the eigenvector radiative transfer equation (8) used here accounts for only one dimension in space (i.e., $\partial u_i/\partial x$), the wave refraction mechanism is not well represented by the source function $\xi^{(a)}$. For example, at depth 9.3 m, where the bottom topography (see Figure 2) suggests that there may be wave refraction caused by the depression in the topography, the corresponding source function $\xi^{(1)}$ does not show any pronounced effect on the magnitude of the function that can be related to the refraction. There seems to be no evidence of wave refraction given by $\xi^{(a)}$.

DISCUSSION

A consequence of fitting the empirical eigenfunction to the data is that the variance is divided according to the eigenvalue based on the orthogonal property. Although the property is inherent in the variance, it does not mean that the processes affecting the variance should have the same orthogonal property. For example the principal eigenvectors of matrix U were replaced by the summations of the eigenvectors corresponding to λ_2 to λ_7 so that the energy transfer associated with the variance, which is orthogonal to the principal axes of the data, can be investigated as demonstrated in the preceding section. The replacement essentially corresponds to the variance partition according to the eigenvalues, where the first matrix U has the principal components of the data and the latter matrix U has the orthogonal variance components. This however, does not necessarily imply that the wave processes associated with the orthogonal variance have the same orthogonal property. In fact the variance partition, according to the eigenvalues, may not be exactly the same amount as the variance attributed to the wave processes. Nevertheless, the results of our study indicate that the variances attributed to various wave mechanisms appear to be reasonably approximated by the variances given by the division of eigenvalues into two major partitions as stated earlier. This is supported by the qualitative agreement between the source functions obtained in our calculations and the source functions resulting from the theoretical analysis of an individual wave mechanism.

The significance of the source functions derived from wave data must be emphasized, since the theoretical source functions may not accurately represent the actual energy transfers of a complicated wave field such as the one measured during the ARSLOE. Because the derivation of the theoretical source functions assumes that certain wave mechanisms occurred in the wave field, the energy balance is constrained by such mechanisms. Thus the accuracy of the energy transfers depends on the accuracy of the assumption made. However, the source functions derived from wave data make no assumption on the processes in the wave field, and therefore, they directly represent the actual wave energy transfers. Furthermore, it should be noted that the wave spectral evolution, as governed by the radiative transfer equation (7), exhibits temporal stochastic and spatial deterministic properties, which can be a basis for stochastic-dynamic modeling for prediction purposes. The temporal forcing, $\partial u_i/\partial t$, can be modeled as a time series autoregressive process so that the advanced spectral evolution in time can be predicted. Expression (8) is valid for the computation of predicted ξ_i. Since the spatial wave dynamics in shallow water depend on the topography of the region, the deterministic part, $\partial u_i/\partial x$, may remain consistent for the area selected. Also notice that such a spatial evolution accounts for the local effects. The predicted ξ_i may be inverted to the predicted source functions, which can then be used to hindcast or forecast the wave spectrum by using the integral form of the radiative transfer equation

$$E(t, x) = E(t_0, x) + \int_{t_0}^{t} \xi(t', x')\, dt'$$

where t' and x' vary along a wave-group trajectory from an initial value t_0, x_0 to the point t, x. Although the above expression does not generally represent the solution of the radiative transfer equation, it indicates how the source functions can be used for spectral wave prediction. The prediction effort, therefore, relies on the knowledge of the source terms. In other words the better approximation of the actual source terms in the wave field will enhance the accuracy of the prediction.

This is why the source functions derived from wave data are very important quantities.

The study has also addressed a lack of the independent source term to represent the energy balance caused by wave breaking. Although this energy balance is accounted for in the source functions $\xi^{(a)}$ and $\xi^{(c)}$, an individual source term for breaking waves is still needed, since it may provide important information for our understanding of the wave-breaking phenomenon. A detailed field experiment over the breaker zone where wave breaking is the most dominant process, together with the application of the present calculations, may provide the wave breaking source function. The function could offer a valuable support to the theoretical investigation of breaking waves, as well as enhance the picture of wave energy transfers in the strongly nonlinear region of the surf zone. In addition a significant deficiency is also found in the study: the lack of a spatial dimension to account for the energy balance caused by wave refraction in two-dimensional space. The refraction process is important in energy transformation, particularly in the wave propagation regime, but it has not been well represented by the source function $\xi^{(a)}$, as shown in the preceding section. Thus an increment of the spatial dimension in the radiative transfer equation could be a useful improvement to the energy balance in the surf zone.

CONCLUSIONS

The frequency wave spectra from ARSLOE were subjected to the empirical eigenfunction analysis. The wave data were acquired in frequency, time, and space domains, but to simplify the analysis, the three variables were reduced to two variables for each computation of the empirical eigenfunction by holding either the time or the space constant. In the case of constant time the data set is in frequency and space domains with the increment according to the time series, and similarly for the constant space, the data set is in frequency and time domains with the increment of various instruments at different depths. All the 52 covariance matrices were fitted by the empirical eigenfunctions. The results suggest that almost 99% of the variance is contained within the first seven eigenvalues, with the first eigenvalue being as high as 80% or more and the remaining values decreasing very rapidly. This implies that the wave field may have the minimum of 7 degrees of freedom with the principal eigenfunctions, which provide a good approximation to the principal structures of the wave field. The spatial variation is found to be approximately 1–3% of the variance, and it could be deterministic, as shown by the eigen index. The temporal variation is estimated at 7–17% of the variance, and it could be stochastic, with approximately 2–3 cycles of fluctuation. The fluctuation is found to be correlated with the variation of the corresponding wind speed. Although the major variabilities in the data are well represented by the principal eigenfunctions, the eigenfunctions associated with each eigenvalue from the second to the seventh values do not provide additional information about the physical wave processes. This is because there are several competing wave mechanisms that are not separable by means of variance partition according to each eigenvalue.

However, since the principal eigenfunction in frequency and space domains can provide a good approximation of the principal frequency wave spectrum, it is used to represent the measured wave field in the radiative transfer equation. The equation is then projected onto the eigenvector space with a suitable projection function, which allows the source function to be solved. The rates of change of the energy density spectra in time and space are available from the empirical eigenfunction analysis, and thus the computations of various source functions were attempted. The calculations demonstrate how the source functions can be evaluated from wave data via the empirical eigenfunction analysis. The analysis is important in the calculations because it provides two essential quantities: a good approximation of the principal frequency wave spectrum and the quantitative spectral evolution in time and space. Because the computed source functions are derived directly from the wave data and have made no assumption on the wave process and their interactions, the functions are direct representations of the actual energy transfers in the wave field. Furthermore, the calculations require no detailed knowledge of the forcing terms or the precise measurement of the wind field, which could be an advantage of the computations.

When the computed source functions are compared with the theoretically derived source functions of known wave mechanisms there are certain similarities as well as differences. The qualitative agreements seem to suggest that the functions are associated with refraction and shoaling, atmospheric input, bottom friction, and wave-wave nonlinear interaction. On the other hand the differences may be attributed to the different wave field environments and circumstances. At various depths it is shown that the computed source functions provide a reasonable picture of the energy balance in the shallow water. In the surf zone it is interesting to note that the nonlinearity at low frequency ($f < 0.25$ Hz) is found to be greater than at high frequency ($f > 0.25$ Hz), whereas beyond the surf zone, the reversed situation is found. This implies that beyond the surf zone the nonlinearity associated with wave growth mechanism is most pronounced, while inside the surf zone the nonlinearity associated with energy dissipation of large wave is most dominant.

Acknowledgments. The work was supported by the National Science Foundaton under contract DAR-8023425. The ARSLOE data were made available to us by the U.S. Army Coastal Engineering Research Center and their cooperation is gratefully acknowledged. It is our pleasure to thank A. J. Willmott for reading the manuscript.

REFERENCES

Aranuvachapun, S., and J. A. Johnson, Beach profiles at Gorleston and Great Yarmouth, *Coastal Eng.*, *2*, 201–213, 1979.

Chambers, Li. G., *Integral Equations: A Short Course*, pp. 22–28, International Textbook Company Ltd., London, 1976.

Ewing, J. A., T. J. Weare, and B. A. Worthington, A hindcast study of extreme wave conditions in the North Sea, *J. Geophys. Res.*, *84*(C9), 5739–5747, 1979.

Günther, H., W. Rosenthal, and K. Richter, Application of the parametrical surface wave prediction model to rapidly varying wind fields during JONSWAP 1973, *J. Geophys. Res.*, *84*(C8), 4855–4864, 1979*a*.

Günther, H., W. Rosenthal, T. J. Weare, B. A. Worthington, K. Hasselmann, and J. A. Ewing, A hybrid parametrical wave prediction model, *J. Geophys. Res.*, *84*(C9), 5727–5737, 1979*b*.

Günther, H., W. Rosenthal, and M. Dunckel, The response of surface gravity waves to changing wind direction, *J. Phys. Oceanogr.*, *11*(5), 718–728, 1981.

Hasselmann, K., Weak interaction theory of ocean waves, in *Basic Developments in Fluid Dynamics*, edited by M. Holt, pp. 117–182, Academic, New York, 1968.

Hasselmann, K., et al., Measurements of wind-wave growth and swell decay during the Joint North Sea Wave Project (JONSWAP), *Deut. Hydrogr. Z., Suppl. A*, *8*(12), 1973.

Hasselmann, K., D. B. Ross, P. Müller, and W. Sell, A parametric wave prediction model, *J. Phys. Oceanogr.*, *6*(2), 200–227, 1976.

Miles, J. W., On the generation of surface waves by shear flows, *J. Fluid Mech.*, *3*, 185–204, 1957.

Phillips, O. M., The equilibrium range in the spectrum of wind-generated ocean waves, *J. Fluid Mech.*, *4*, 426, 1958.

Preisendorfer, R. W., F. W. Zwiers, and T. P. Barnett, Foundations of Principal Component Selection Rules, *SIO Ref. Ser. 81-4*, pp. 21–46, Scripps Inst. Oceanogr., Univ. Calif., San Diego, 1981.

Ribe, R. L., Calibrations and energy spectrum correction factors for waverider buoys deployed under the ARSLOE program, *ESO Tech. Rep. TE 3-81-012*, p. 63, Eng. Support Off., Ocean Technol. Eng. Serv., NOAA, Wash., D. C., 1981.

Shemdin, O., K. Hasselmann, S. V. Hsiao, and K. Herterich, Nonlinear and linear bottom interaction effects in shallow water, Turbulent Fluxes Through the Sea Surface Wave Dynamics and Prediction, edited by A. Favre and K. Hasselmann, *NATO Conf. Ser. 5*, Air-Sea Interaction, vol. 1, pp. 347–372, NATO, Marseille, France, 1978.

Thornton, E. B., and R. T. Guza, Energy saturation and phase speeds measured on a natural beach, *J. Geophys. Res.*, *87*(C12), 9499–9508, 1982.

Vincent, C. L., and D. E. Lichy, Wave measurements in ARSLOE, paper presented at Conference of Directional Wave Spectra Applications, Am. Soc. Civil Eng., San Francisco, Calif., 1982.

Vincent, C. L., and D. T. Resio, An eigenfunction parameterization of a time sequence of wave spectra, *Coastal Eng.*, *1*, 185–205, 1977.

Wallace, J. M., and R. E. Dickinson, Empirical orthogonal representation of time series in the frequency domain, Part 1, Theoretical consideration, *J. Appl. Meteorol.*, *2*, 887–892, 1972.

Wang, D-P., and C. N. K. Mooers, Long coastal-trapped waves off the west coast of the United States, Summer 1973, *J. Phys. Oceanogr.*, *7*(6), 856–864, 1977.

S. Aranuvachapun, Institute of Oceanographic Sciences, Crossway, Taunton, Somerset TA1 2DW, United Kingdom.

E. B. Thornton, Department of Oceanography, Naval Postgraduate School, Monterey, CA 93943.

(Received February 22, 1983;
revised March 1, 1984;
accepted March 6, 1984.)